Plasmonics
https://doi.org/10.1007/s11468-024-02458-3

RESEARCH

Plasmonic Metamaterial's Light Trapping Enhancement of Ultrathin PbS-CQD Solar Thermal PV Cells

Oussama Baitiche[1] · Fathi Bendelala[1] · Ali Cheknane[1] · Filippo Costa[2] · Hikmat S. Hilal[3] · Jean-Michel Nunzi[4] · Khadidja Younes[1]

Received: 24 May 2024 / Accepted: 24 July 2024

Abstract
Enhancing photon absorptance in ultrathin solar/thermophotovoltaic (STPV) cells is crucial for low-cost highly efficient cells. A complete study of power conversion enhancement, in a proposed ultrathin STPV cell, is presented here. It involves lead sulfide colloidal quantum dots (PbS-CQDs), a silver (Ag)-nano-pyramid design, aluminum nitride (AlN) crossed prisms as front texturization, with embedded Ag nanospheres, and a tantalum (Ta) film as a back reflector. By combining the three mechanisms of surface plasmon polariton (SPP), localized plasmons (LSPR), and magnetic polariton (MP) in the same structure, photon absorptance in the active PbS-CQDs layer is greatly improved. The suggested structure attained a highly active absorptance of over 80%, covering visible and near-infrared (0.30–1.77 µm). The short circuit current density is also evaluated under AM 1.5 solar illumination and various blackbody temperatures (T_B), with values of 48.90 mA cm^{-2} and 6.93 mA cm^{-2}, respectively, corresponding to unprecedented power conversion efficiencies (PCEs) of 20.20% and 15.58%. The effects of metamaterial light management on PCE enhancement are discussed. Collectively, the findings show that the proposed hybrid cell is potentially useful in high-performance hybrid thermal and solar cells.

Keywords Metamaterial · Hybrid solar cell · Thermophotovoltaic · PbS colloidal quantum dot · Plasmonics · Light trapping

Introduction

Recently, research on quantum dot (QD) solar cells became active by virtue of their special features including lightweight, low cost, multiple exciton generation (MEG) benefit, and bandgap tunability [1]. However, their low power conversion efficiency (PCE), typically below 20%, is their major challenge [2, 3]. Research is thus active to improve the functionality and performance of QD solar cells. Light management—a term that encompasses any technology used to raise the optical efficiency of the solar thermophotovoltaic (STPV) conversion—is typically an excellent way to address these issues. A coating or a textured anti-reflection layer is used to improve light in-coupling at the front [4]. A back reflector is used to avoid leakage of light from the back side [5]. Moreover, texturing interfaces are used to improve light dispersion. This enhances the light path within the absorbing layer [6]. Introducing spherical gold nanoparticles to the absorber layers of perovskite solar cells improved incident radiation capturing in photovoltaic devices [7, 8]. Controlling the photonic structures and plasmonic nanoparticles exhibited significant effects on efficiencies of perovskite solar cells [9]. Simulation results showed that the geometry affects the absorption efficiency, where values higher than 99% were obtained in simple harmonic absorbers involving gold reflectors [10].

The trend of nanostructured metamaterials (MTM) is the most widely utilized approach in light management [11], particularly through surface plasmon polariton (SPP) and transverse magnetic polarization (TM) or p-polarized light. SPP appears at the metal/dielectric interface [12] with two typical coupling configurations, namely Maier [13]. Common plasmonic materials can be classified into two

Highlights
- An ultrathin solar/thermophotovoltaic cell involving lead sulfide colloidal quantum dots is proposed.
- The cell shows a highly active absorptance > 80% in visible and near IR.
- The cell exhibits PCE values of 20.20 and 15.58% under AM 1.5 solar and various blackbody temperatures.

Extended author information available on the last page of the article

Published online: 13 August 2024

categories based on the resonances they support. The first category includes materials with a real part permittivity that is negative and greater than either the imaginary and real part permittivity of the neighboring medium. The second type appears when the permittivity real part is positive and greater than its imaginary part, as well as the permittivity of the medium around it [13].

Moreover, enhancing charge carrier diffusion and extraction, together with lowering recombination in STPV cells, requires a reduction in active layer thickness (< 100 nm) [14]. This is due to the fact that the maximum thickness of the active layer, typically between 200 and 300 nm, is dictated by the diffusion length of QD active layers. Light trapping in nanostructures was described as an efficient approach to optimize solar cell performances [15]. Several nanostructured mechanisms have been used to trap light in STVP conversion thin active layer, namely plasmonic nanoparticle structures [16, 17], arbitrary scattering surfaces [18], periodic nano-grating [19, 20], nanowires [21], and photonic crystal structures [18, 22]. However, developing low-cost and efficient low-bandgap cells is critical to simultaneously develop a thermal and solar conversion system, namely a hybrid STPV cell [23]. Colloidal quantum dots (CQDs) (i.e., PbS and PbSe) are promising candidates for hybrid STPV conversion [10, 24]. This phenomenon is due to the absorptance bandgap of solid-state PbS, being located within the infrared range (~ 0.4 eV), which can be adjusted by controlling QD synthesis conditions [25]. Moreover, PbS-CQD technologies have already shown external quantum efficiencies (EQEs) of over 100% reached through the MEG advantage [26]. According to a recent report, the PCE for PbS-CQD-based solar cells reached above 10% [27]. Lan et al. reported a PCE of 10.6% for a PbS-CQD cell using solvent-polarity-engineered halide passivation [28]. Hong et al. used an alternating D-A copolymer hole transport layer to achieve a PCE of 14% [29]. By introducing an organic layer, Ding et al. [30] reported a PCE of 15.45%. However, further improvement is still being aspired.

PbS QDs are low-cost and easy-to-prepare materials. However, Pb ions are environmentally hazardous [31]. For PbS, this is also well documented based on its MSDS and literature. Fortunately, this difficulty is relaxed by the fact that PbS has a very small solubility product of 3.2×10^{-28} under neutral conditions. Therefore, the environmental concerns associated with PbS can be avoided by green chemistry practices. Natural waters are being contaminated with lead ions, from various processes such as lead-acid battery [32], lead plumbing, and other industrial processes [33, 34]. One way is to prepare PbS films by simple depositions from lead ions in contaminated waters [35, 36]. Thus, PbS-based QD technology can be virtuous in the sense that waters pre-contaminated with lead ions can be used in manufacturing the QDs.

This study proposes a hybrid solar/thermal cell enhanced by a nanostructured plasmonic metamaterial that could potentially be used at the ultrathin absorber layer to boost light trapping and conversion efficiency. The suggested cell involves silver truncated pyramids, and AlN cross prisms on a cell surface, with an ultrathin active layer of PbS-CQDs having a low bandgap of $E_g = 0.7$ eV and supported by silver nanoparticles (Ag-NSs). Additionally, the active layer is backed by a tantalum (Ta) film. The diverse plasmonic phenomenal attributes of emerged nanostructures incorporated in the ultrathin cell are calculated using the method of finite difference time domain (FDTD) under solar (AM 1.5) and various blackbody source radiation. The optical and electrical performances of the proposed design will be compared to conventional cells of similar nature. The unique technique is a new attempt to lower lead toxicity by minimizing the harmful PbS substance in the cell. Simultaneously, the power conversion will be improved. The implications of plasmonic metamaterial light management enhancement are examined. The proposed structure has an active absorptance of approximately 80% along a broadband spectrum (0.30–1.77 μm). This eventually affects the cell short circuit current density (J_{sc}). Under AM 1.5 sun, and at different blackbody temperatures, J_{sc} values of 48.90 and 6.93 mA cm^{-2}, respectively, are obtained. As a result, the PCE values are 20.20% and 15.58%, respectively.

Materials and Methods

The optoelectronic study of the suggested hybrid PbS-CQDs STPV cell uses FDTD numerical methods based on Maxwell's equations. As this approach is often the most robust option for curved or highly dynamic surfaces, it enables modeling wide ranges [37, 38]. Thus, optical and electronic studies will constitute the two complementary directions for the current research. Table 1 includes a complete list of material properties for device physics modeling.

Analyzed Structure and Optical Analysis

All CQD photovoltaic devices described to date have absorption that is significantly lower than unity across the whole above-bandgap spectrum. Physical, chemical, and optical approaches have been used to improve the overall absorption of CQD solar cells [43]. The absorption issue is particularly noticeable in CQDs with narrower bandgaps (when $E_g < 1.0$ eV). This significantly limits the efficiency of IR-CQD devices. Increasing the thickness of the CQD layer results in reduced efficiency of excited photocarrier extraction. The active layer thickness is currently limited to the total drift and diffusion lengths, and further expanding it results in greater recombination and decreased overall

Table 1 Material parameters used in the optoelectronic simulation of the suggested hybrid PbS-CQDs STPV cell, based on literature

Parameters	PbS [39]	Ag [40]	AlN [41]	Ta [42]
Work function (eV)	4.60	4.26	6.0	4.19
Electron affinity (eV)	3.8	1.304	0.6	0.328
Bandgap (eV)	0.7	-	6.2	-
Electron/hole mobility $\mu_{e,h}(\mathrm{cm}^2/\mathrm{V.s})$	0.01	-	-	-
Electron/hole lifetime $\tau_{e,h}(s)$	2×10^{-7}	-	-	-
Relative permittivity ε_r	18	-	8.5	-
Doping (cm^{-3})	10^{16}	-	-	-

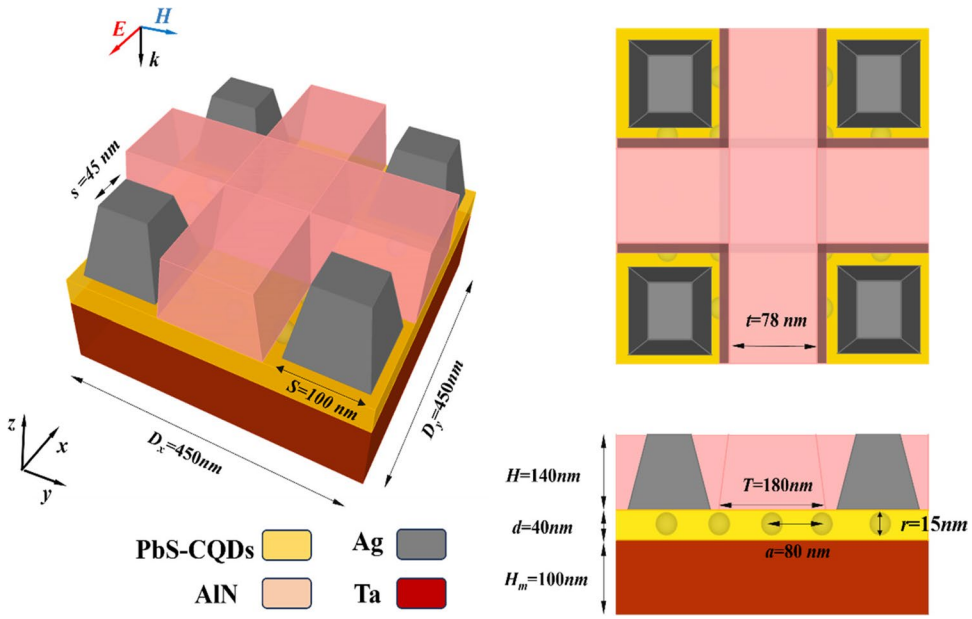

Fig. 1 The architecture of the proposed hybrid STPV cell

conversion performance. The suggested configuration is founded upon a nanostructured hybrid PbS-CQD STPV cell comprising a succession of strata organized from the uppermost to the lowermost levels. To avoid the previously mentioned issues, absorption improvement demands an ultrathin active layer, as depicted in Fig. 1. Silver exhibits the LSPR and MP phenomena; PbS is the most commonly used CQD for thermophotovoltaic applications because it is a low-cost material that was considered an absorber layer [44]. Three light trapping strategies have been used in this study: light trapping near the top surface (Ag-pyramid), trapping near the bottom surface (Ta), and another light-confinement mechanism around the embedded nanoparticles (Ag-NSs).

Four Ag truncated pyramids are located at the corners of the configuration, paired with cross-shaped AlN prisms for frontal texturization, an ultrathin layer of PbS-CQDs enhanced by Ag-NSs acting as the absorber layer, and a Ta back contact. The Ta layer is assumed to be $Hm = 100$ nm thick. Ag and AlN structures are $H = 140$ nm in height, with an active layer thickness of $d = 40$ nm. Optical proprieties of materials were modeled from available experimental data using the multi-coefficient fitting tool within the simulation software [45, 46]. Ag-NSs, embedded in the active layer with a radius of $r = 15$ nm, are in a lattice-like deposition of $a = 80$ nm distance in the x- and y-directions. The unit cell dimensions are $Dx = Dy = 450$ nm in the x- and y-directions. The incoming light is regarded as a plane-wave source, and the simulation wavelength span is set at 0.3–2.5 µm, since PbS-CQDs STPV cells currently need absorptance enhancement in this spectral range. It is possible to set up specific boundary conditions, like perfectly matched layer (PML) boundaries in the z-direction and periodic boundaries in both x- and y-directions. This reduces the infinitely large periodic structure to a small model unit cell. The total absorptance ($A_T = 1 - R - T$) is computed [38], where R and T represent the total reflectance and transmittance of the unit cell.

Additionally, each layer's energy absorption per unit volume (P_{abs}) can be calculated using Eq. (1) [47]:

$$P_{\mathrm{abs}} = \frac{1}{2}\varepsilon_0\varepsilon_i'' w\left|E_i\right|^2 \tag{1}$$

where ε_0 is vacuum permittivity, describes the electric field inside the layer (i), and describes the imaginary component of permittivity for the chosen layer (i), and is the angle

frequency [47]. Absorbed power, within each layer, can be standardized to incident power to have the absorptance at layer (i) (Eq. (2))

$$\alpha_i = \frac{\int P_i dV_i}{0.5 c_0 \varepsilon_0 \left|E_{\text{inc}}\right|^2 A} \tag{2}$$

where E_{inc} denotes the incoming electric field, and c_0 is light velocity. $\boldsymbol{A}$ represents the area subject to incident light, V_i describes the volume for the given layer i, and the total power absorbed by the entire structure ($\int P_i dV_i$) can be expressed as the aggregate of the energy absorbed by individual layers.

Electronic Study

To evaluate the electronic properties of the proposed structure, values of open-circuit potential (V_{oc}), short circuit photocurrent density (J_{sc}), output electric power (P_{out}), total incident radiative flux $\boldsymbol{P_{in}}$, and electric power generated by the cell (P_{cell}) should be determined. The short circuit current density as an electrical output parameter has been obtained using Eq. (3) [47]:

$$J_{sc} = \int_0^{\frac{hc_0}{E_g}} \frac{q\lambda}{hc_0} \alpha(\lambda) QE(\lambda) E_{b\lambda}(\lambda) d\lambda \tag{3}$$

where h is Planck's constant, q is an elementary charge, E_{g} is the bandgap (0.7 eV) for PbS-CQDs. QE(λ) and α(λ) describe the quantum efficiency and the absorbed power of the active layer, respectively. When the cell is used as a solar converter, the radiative heat flux is defined as AM 1.5 solar radiation, and a blackbody source for TPV applications. Radiative heat flux, from a blackbody emitter, is computed according to Eq. (4) [48]:

$$\mathrm{E_{b\lambda}(T_B)} = \frac{\mathrm{C_1}}{\lambda^5 \left[\exp(\mathrm{C_2}/\lambda \mathrm{T_B}) - 1\right]} \tag{4}$$

where $C_1 = 3.742 \times 10^8 \mathrm{W}\mu\mathrm{m}^4/\mathrm{m}^2$, $C_2 = 1.439 \times 10^4 \mu\mathrm{mK}$, and T_{B} describes blackbody temperature.

The ratio of $\boldsymbol{P_{\text{cell}}}$ to $\boldsymbol{P_{\text{in}}}$ can be used to express the cell PCE (η) by Eq. (5) [49].

$$\eta = \frac{P_{cell}}{P_{in}}.100\% \tag{5}$$

To compute PCE, it is necessary to compute P_{in} and P_{cell}. The value of total incident radiative flux $\boldsymbol{P_{\text{in}}}$ on the STPV cell is then computed according to Eq. (6) [47]:

$$P_{in} = \int_0^{\infty} E_{b\lambda}(\mathrm{T}) \varepsilon_\lambda d\lambda \tag{6}$$

where ε_λ is the emissivity of the intermediate emitter. The output electric power of the cell ($\boldsymbol{P_{\text{cell}}}$) is determined by Eq. (7) [50]:

$$P_{cell} = J_{sc} V_{oc} FF \tag{7}$$

where the fill factor (FF) can be estimated by Eq. (8) [50]:

$$FF = \frac{\frac{V_{oc}}{V_t} - \ln\left(\frac{V_{oc}}{V_t} + 0.72\right)}{\frac{V_{oc}}{V_t} + 1} \tag{8}$$

V_t represents the thermal voltage and is defined by Eq. (9) [51]:

$$V_t = \frac{K_B T_c}{q} \tag{9}$$

where T_c represents the cell temperature, and k_B is the Boltzmann constant.

The open-circuit voltage formula is given by Eq. (10) [47]:

$$V_{oc} = \left(\frac{k_B T_c}{q}\right) \ln\left(\frac{J_{sc}}{J_0} + 1\right) \tag{10}$$

where $J_0 = 1.17 \times 10^{-4}\ \mathrm{mAcm}^{-2}$ is the dark current reported earlier [52].

Numerical Results and Discussion

Numerical results obtained with optical electromagnetic analysis are initially presented. Subsequently, the obtained absorption performances are elaborated by using the described theoretical framework to obtain the electronic performance of the proposed structure.

Optical Analysis

Optical analysis is separated in different subsections. It involves the normal incidence absorption performance, the absorption mechanisms, the parametric analysis, and finally the behavior of the absorbing structure as a function of the incidence angle.

Absorbed Power

The proposed optimized design shows a wide range (0.30 to 1.77 μm) in normalized absorptance plotted under transverse electric (TE) and transverse magnetic (TM) incident waves. The light absorptance is optimal, with a value of 99%. Furthermore, it is appropriate for the designated range of the cell (with energy > E_{g}), and the symmetry of the unit

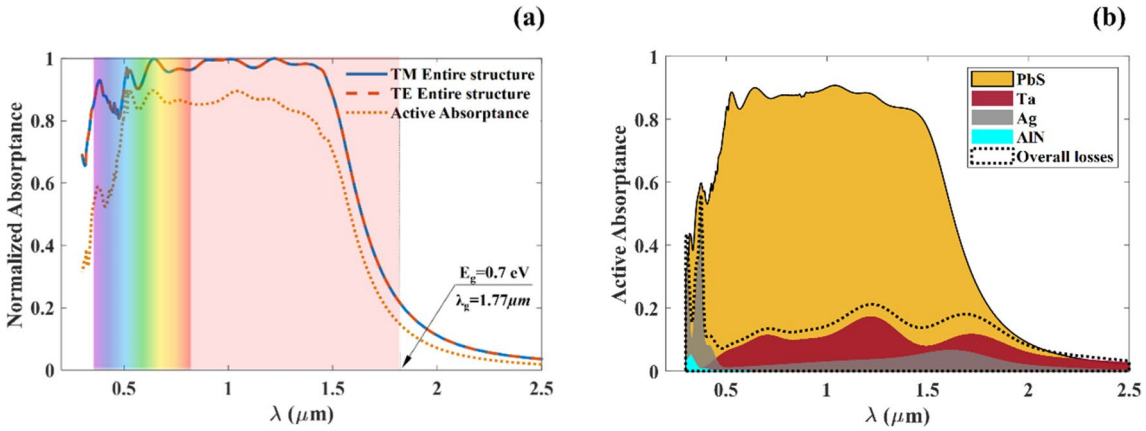

Fig. 2 Normalized calculated absorptance spectra using the FDTD approach. **a** Full design and active layer absorptance **b** active absorbed power compared with loss power per material

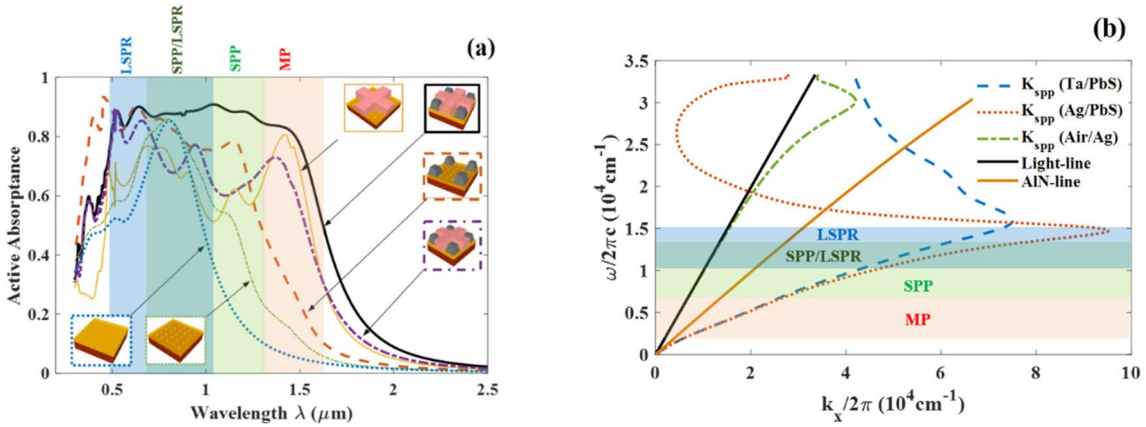

Fig. 3 Effects of various structures on PbS-CQD spectral properties. **a** Absorptance spectra, **b** plasmonic dispersion curves at the different metal/dielectric interfaces

cell under normal incidence makes polarization independence easy to achieve, as shown in Fig. 2a. The simulations have been performed using the optical properties of widely used PbS-CQDs, with a low-bandgap value of 0.7 eV [53].

Figure 2b shows the normalized absorptance spectra calculated using Eqs. (1) and (2) in various materials (PbS-CQDs, Ag, Ta, and AlN). Energy is mostly (81%) absorbed by the PbS-CQDs active layer, with 19% overall loss, ranging from 0.3 to 2.5 µm, by other materials. The absorption mechanisms are studied in the following section.

Absorption Mechanisms

Figure 3a depicts the evaluation of the effect of different structural components. It is clear that bare PbS-CQDs cell, single element of crossed prism cell, pyramid texturization or embedded Ag-NSs, cannot separately achieve considerable absorptance, especially at infrared wavelengths. However, a strong synergistic interaction between these parts is observed once these five structures are combined in the same design. This is also achieved through the meticulous manipulation of the structure geometric parameters, resulting in plasmonic excitation regulation within the active layer.

Several plasmonic MTM mechanisms can potentially improve the light absorptance of the PbS-CQDs layer [54]. Three types of near-field scattering are considered, namely localized surface plasmon resonance (LSPR), magnetic polariton (MP), and surface plasmon polariton (SPP). The LSPR refers to a non-propagating surface plasmon excitation where electrons oscillate due to radiation, resulting in an intensified electric field around nanoparticles or limited surfaces. Ag-NSs improve light absorptance due to the increased near-field energy in the active layer (zone in blue).

In contrast, the SPP waves propagate along dielectric and metal interfaces. The dispersion relation given by Eq. (11) is numerically computed in Fig. 3b that represents the

dispersion relation of the surface waves. This relationship establishes the mechanism of plasmonic wave excitation in such a configuration [55].

$$k_x = \frac{\omega}{c}\sqrt{\frac{\varepsilon_m \cdot \varepsilon_d}{\varepsilon_m + \varepsilon_d}} \tag{11}$$

where k_x is the x-component of the SPP wave vector, ε_d, and ε_m are the dielectric functions of the metal and dielectric, respectively, with opposite signs to excite plasmonic modes; c is the speed of light in air, whereas ω represents the angle frequency. According to Fig. 3b, the wavelength of SPP at the Ag/PbS and Ta/PbS interfaces is shorter than the incoming light wavelength (light line). This enhances the magnetic field intensity in the PbS-CQDs layer because the extension of the SPP resonances is noticed to reach broadband resonance due to the higher order modes of the SPP excited at various interfaces (Ag/PbS and Ta/PbS). Nevertheless, the dispersion curve of SPPs in a planar interface typically resides to the right of light line, due to evanescent wave characteristics. Excitation of SPPs can be achieved using propagation waves and periodic gratings, as the Bloch-Floquet condition [47] allows for the matching of large in-plane wave vectors with high-order diffracted waves (Eq. (12)):

$$k_{x,j} = k_x + 2\pi \mathrm{j}/D_x \tag{12}$$

where D_x represents the cell periodicity in the x-direction, j represents the x-direction diffraction order, and $k_x = \omega/c$ denotes the parallel component of the in-vacuum wave vector.

For SPP modes, the resonance frequency can be theoretically determined by solving for $\left|k_{spp}\right| = \left|k_{x,j}\right|$. As a result, an increase in light absorptance is anticipated, as shown by the green zone in Fig. 3. Depending on their power, SPPs typically spread between 10 and 100 nm along the interface [56]. Sandwiching the PbS-CQDs layer, between Ag-pyramids and Ta back layer, supports a strong plasmonic magnetic polariton (MP). Earlier studies reported conflicting understandings of the physical processes of the MP modes. Ortuno et al. investigated the role of SPPs in optical transmission through double-layer metallic-hole arrays. They speculated that MP mode is excited by the coupling of internal SPPs, but did not provide additional explanations [57]. Lee et al. assumed that the MP was induced by magnetic elements, produced in the structure, based on Lenz's law not by the internal SPPs [58]. Wang et al. stated that magnetic resonance can be excited to create MP at a defined wavelength with a particular set of parameters [59]. The explanation provided by Cheng Shuai et al. states that a time-varying magnetic field is necessary for the induced MP in a mechanism. Lenz's law states that this time-varying magnetic field can create closed loops in metallic/dielectric/metallic arrangements before inducing electric current. Strong coupling between SPP modes, created by the upper and lower metal/dielectric interfaces, results from resonance formed when the overall impedance, in the closed loop of electric current, is zero. This leads to a powerful electromagnetic field confinement, thus causing the MPs to be induced between the two interfaces [60]. MPs are localized non-propagating modes that resemble LSPR modes, also known as localized-magnetic plasmon-polaritons (LMPPs) [61]. To the authors, two electrostatic optical-absorptance natures have been excited here: LSPR and MP for visible and infrared regions, respectively. LSPR is induced when $k_x \to \infty$, and SPP group velocity $vg \to 0$ (non-propagating waves). Due to the metal damping, $kx \to \infty$ is impractical.

For the mid-infrared region or lower, the $k_{spp}(Ta/PbS) \approx k_{spp}(Ag/PbS)$. Thus, the dispersion curves are consistent with a linear behavior. Here, waves cover a wide range of interfered SPP wavelengths and, furthermore, can propagate at the same speed. All of these mechanisms can contribute to MP mode excitation in this wavelength range (zone in red). As a result, the intersection band between the green and blue zones is due to the coupling of SPP with LSPR modes appearing in the region between Ta/PbS contact and Ag-NSs, respectively. The AlN-prism significantly contributes to the excitation of the previous three plasmonic MTM phenomena via converting normal incidence to oblique incidence. It also increases the path length in the active layer along the metal/dielectric interfaces, as illustrated in Fig. 3a.

Furthermore, FDTD is used to calculate the electromagnetic field distribution at wavelengths of $\lambda_1 = 1.489$, $\lambda_2 = 1.280$, $\lambda_3 = 1.000$, and $\lambda_4 = 0.675$ µm for two adjacent cells, to clarify the underlying plasmonic MTM mechanism (Fig. 4). The absorptance at $\lambda_1 = 1.489$ µm is associated with the MP resonance in the Ag/PbS-CQDs/Ta configuration, which leads to intense confinement of light in the active layer. The presence of the top Ag-pyramid modifies the two adjacent plasmonic resonances from SPP to MP under certain circumstances, as discussed earlier (Fig. 4a). On the other hand, Fig. 4b depicts that the second mechanism located at $\lambda_2 = 1.280$ µm is actually due to the SPP excitation in the Ta/PbS-CQDs interface. The Ag-NSs act as antennas at wavelength $\lambda_3 = 0.675$ µm that store the incident light efficiently and re-radiate it in the active layer (Fig. 4d). The small size of Ag-NSs leads to high competence due to their low albedo [54]. This technique is beneficial for materials with required very short carrier diffusion length (i.e., PbS-CQD active layer). This explicates why the Ag-NSs are embedded in the ultrathin film STPV cell, where photogenerated carriers are collected. Otherwise, photogenerated carriers may combine before separation, where the absorbed energy dissipates as ohmic damping. The coupling between the LSPR and SPP waves is clearly visible at $\lambda_4 = 1.000$ µm (Fig. 4c). Studying the scattering mechanism of this configuration under intense incoming waves is actually too hard. That is due to complicated coupling resonances of the three different types of plasmonic resonances over a broadband of absorptance.

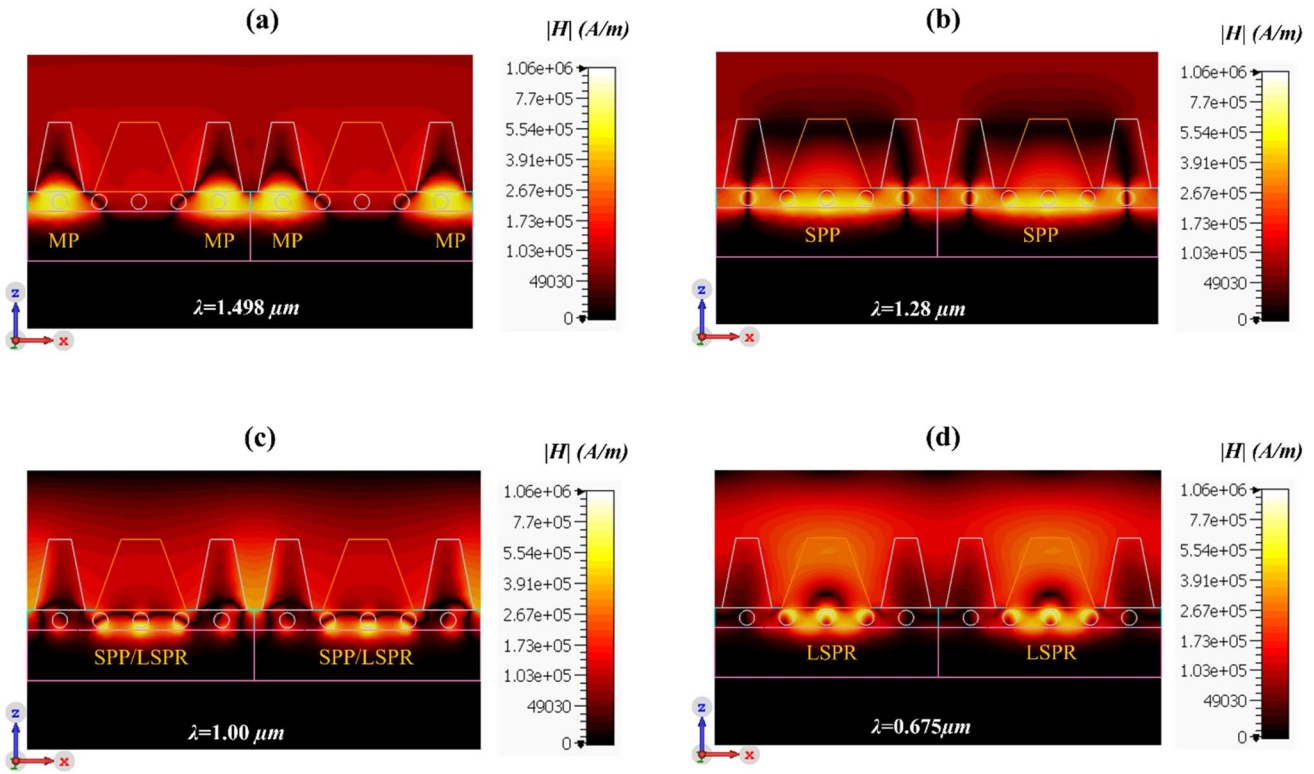

Fig. 4 Distributions of electromagnetic fields at wavelengths consistent with plasmon resonance. **a** Magnetic polariton (MP). **b** Surface plasmon polariton (SPP). **c** Localized surface plasmon (LSPR) and SPP correlated mode. **d** LSPR mechanism

Geometric Parameter Dependence

Figure 5 illustrates how geometric parameters affect the absorptance bandwidth and the plasmonic resonance wavelength. As shown in Fig. 5a, the active layer thickness d is an important parameter to tune the active absorptance rate, particularly concerning the longer wavelengths (IR). This is because the SPP and MP, produced in the active layer, are significantly impacted by variations in "d." Fig. 5b, showing a plot of absorptance versus height (H) of both upper structures Ag-pyramid and crossed AlN-prism, indicates that the SPP and LSPR/SPP strengths gradually decrease with increased H. This has an immediate impact on the absorption rate. The calculation of fill ratio (f_i) entails the division of the overall Ag-NSs volume by the active layer volume. This parameter plays a crucial role in enhancing the absorptance for broad wavelength ranges since the active layer thickness and Ag-NSs density can both be represented by this parameter, as shown in Fig. 5c.

Oblique Incidence Sensitivity

The active absorptance has been computed as a function of wavelength (λ) and incidence angle (θ) (Fig. 6). The active absorptance for TM incidence demonstrates highly insensitive behaviors at oblique incidence. The MP and LSPR mechanisms remain around 0.89 for θ values up to 70°, but SPP and SPP/LSPR absorptance rate drops to 0.75 at $\theta = 60°$.

Furthermore, under TE polarization, SPP and LSPR maintain absorptance rates of about 0.80 for θ up to 70°, whereas MP and SPP/LSPR strengths decrease at oblique TE incidence. That is because the magnetic field, parallel to the frontal texturization, decreases at large incidence angles with TE polarization. MP modes in 1D and 2D texturization can only be induced by the incidence of TM or p-polarized waves. That is to meet the condition that the magnetic field should be parallel to the direction of the texturization. Therefore, despite the incidence angle, the magnetic field value of an incident TM wave is parallel to the grating texturization direction. This explains the insensitivity to the incidence angle. For energy conversion systems such as TPV, this makes it a desirable option. In general, the present findings confirm that TM polarization is less sensitive than TE polarization in the proposed configuration.

Electronic Analysis

Using the equations discussed in the "Materials and Methods" section, the electronic analysis has been examined in

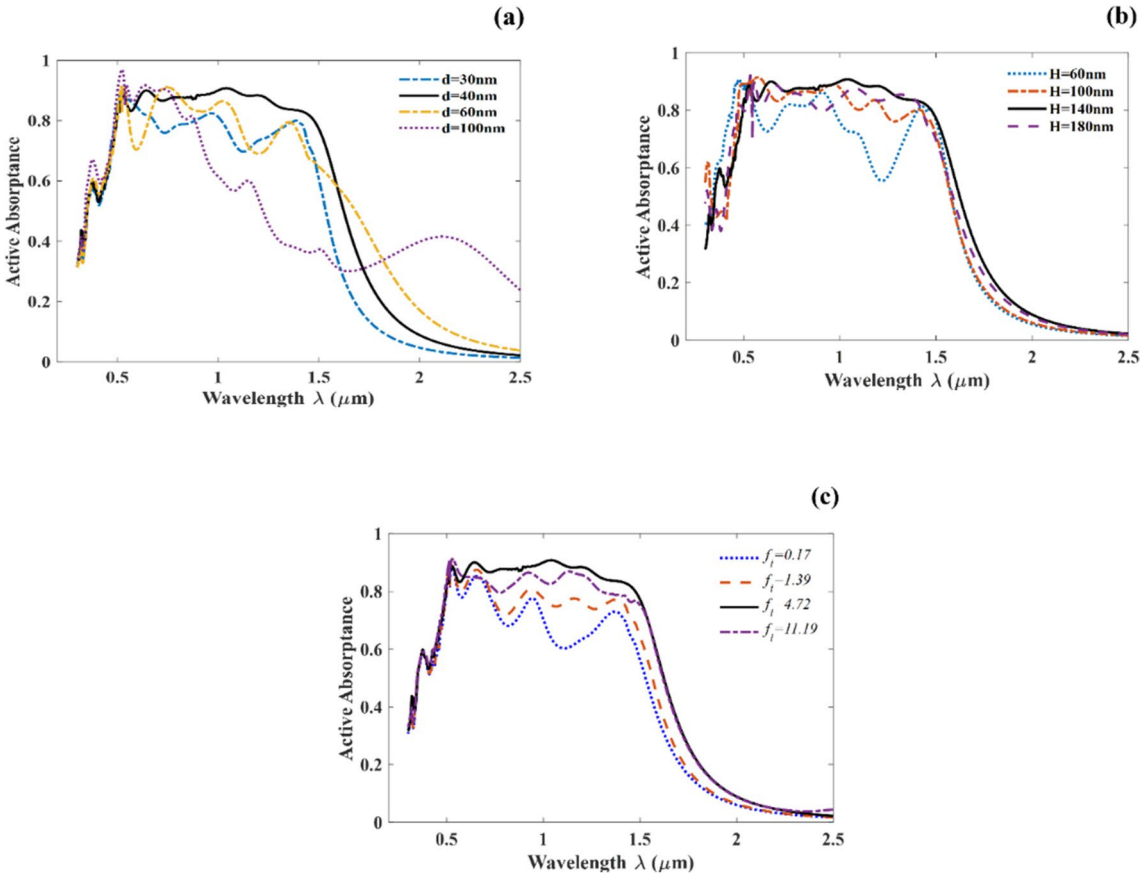

Fig. 5 Active absorptance spectra of the hybrid STPV structure with varying **a** active layer thickness *d*, **b** upper structure height H, and **c** filling ratio of Ag-NSs/PbS-CQDs layers

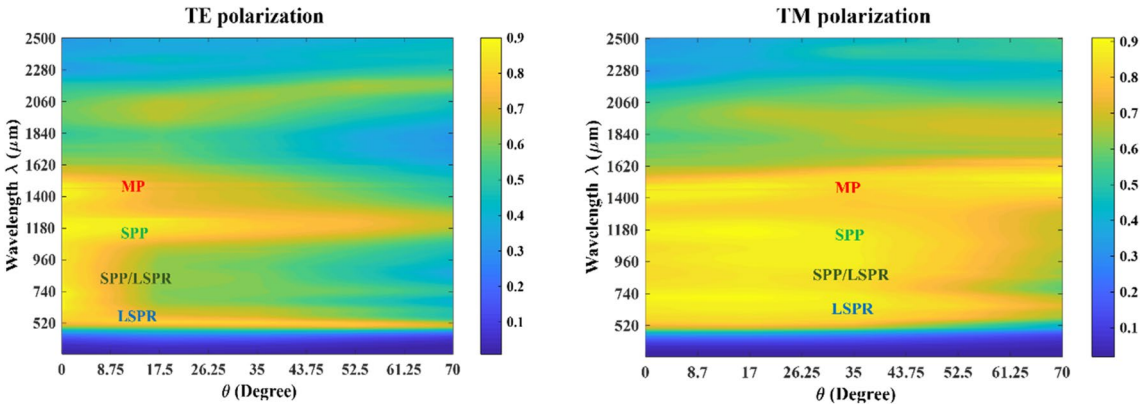

Fig. 6 Diagram of absorbed energy in PbS-CQDs layer with TE and TM polarizations at different incidence angles

order to more clearly demonstrate the impact of the optical absorbance enhancement on the electronic performance of the proposed design. Two power sources have been used to characterize the thermophotovoltaic and photovoltaic outcomes: blackbody radiation and solar radiation AM 1.5. When all carriers are collected, QE is equal to absorptance. However, due to parasitic absorptance, carriers cannot be fully collected. Thus, the QE of an ultrathin solar cell with an absorbing layer and additional functional layers can be estimated by Eq. (13) [62],

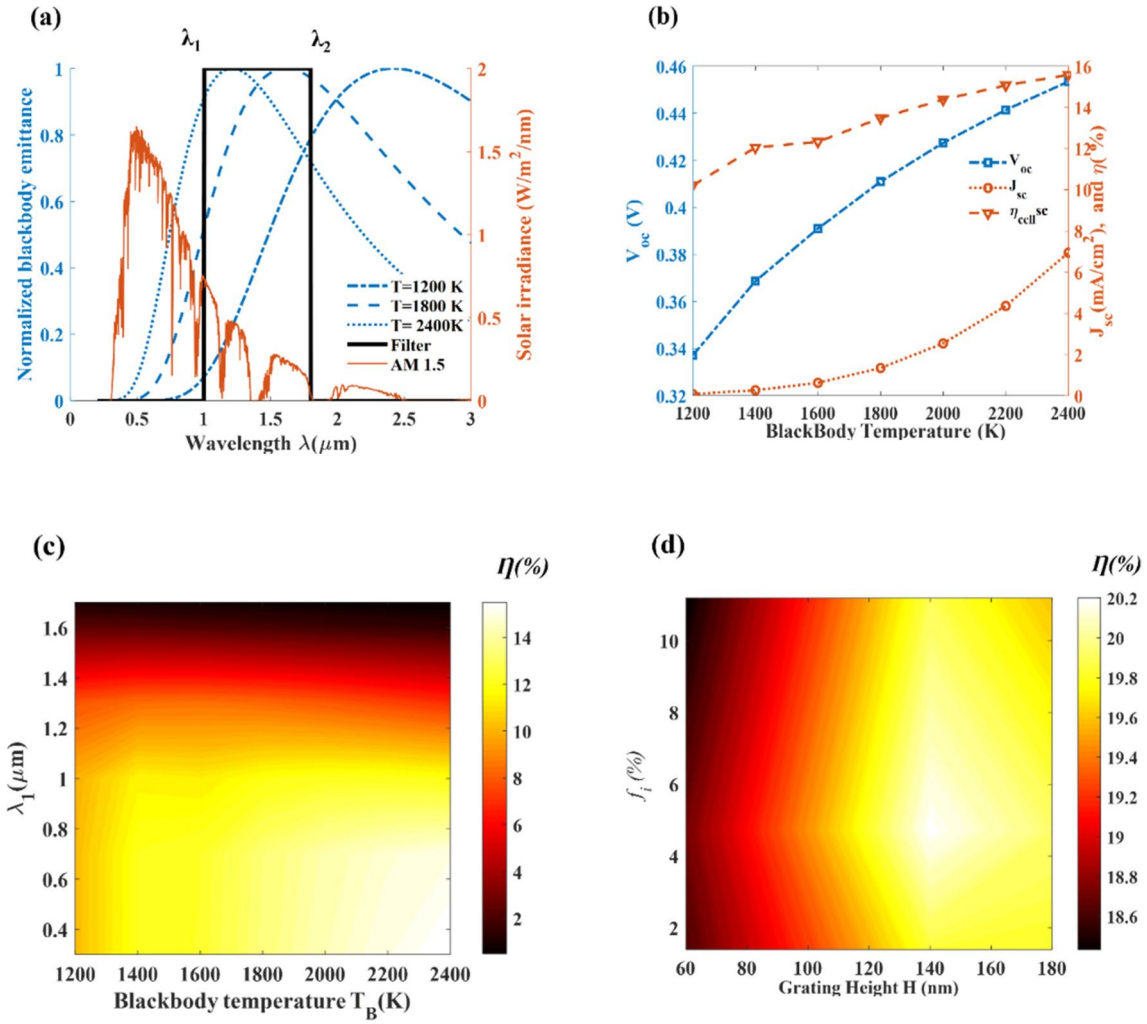

Fig. 7 Proposed cell characteristics calculated under various conditions. **a** Spectral distribution for power fluxes from different power sources with a spectral-ideal filter for a TPV conversion; **b** effect of blackbody temperature on J_{sc}, V_{oc}, and η; **c** effect of both blackbody temperature and λ_1 on PCE (η); **d** influence of both geometric parameters H and f_i on PCE (η)

$$QE = 1 - R - A_p \tag{13}$$

where A_p stands for the parasitic absorptance of the cell front and back layers that can be determined using the optical analysis mentioned above, and R is the overall reflectance. Figure 7a displays the spectral emittance of the ideal TPV filter, which is a window of the chosen wavelength range from λ_1 to λ_2, as well as the normalized blackbody power emittance from a blackbody (at temperatures 1200 and 2400 K) and the solar spectrum (AM 1.5). The PbS-CQDs bandgap is correlated with the fixed cutoff wavelength λ_2 set at 1.77 μm. In contrast, the variable cutoff wavelength λ_1 affects the cell performance. An intermediate filter is an essential component in STPV conversion to decrease excess energy (above the bandgap) and prevent wasted photons with energy below the bandgap, which are unable to produce electron–hole pairs or increase PCE [63]. The filter is also needed to tune the carrying capacity of the cell [47].

Table 2 shows a comparison between characteristics for the proposed hybrid TPV cell and literature counterparts with low-bandgap cells, ($E_g = 0.7$ eV), in terms of J_{sc}, V_{oc}, FF, and η. The calculations have been done with $\lambda_1 = 0.3$ μm and under two distinct power sources, blackbody ($T_B = 1300$ K) and solar irradiation (AM 1.5).

Combining several plasmonic MTM processes (LSPR, SPP, and MP) can increase J_{sc} by improving photon absorptance rate across a wide range of wavelengths, directly impacting the cell performance. The J_{sc}, V_{sc}, and FF values were reported by Bi et al. [64] and by Li et al. [65], for AM 1.5 illumination (Table 1). Furthermore, Yu et al. reported a TPV efficiency of 6% at $T_B = 1300$ K. Recently, Ding et al. [30] achieved a maximum PCE of $\eta = 15.45\%$ by introducing organic films of PMMA: PCBM. In contrast, the proposed structure with ultrathin active layer (40 nm) yields higher values of $J_{sc} = 48.9$ mA/cm^2, $V_{oc} = 0.5$ V, $FF = 79\%$, and efficiency $\eta = 20.2\%$ under AM 1.5. Moreover, an outstanding

Table 2 Cell characteristics (V_{oc}, J_{sc}, FF, and PCE) calculated for related various low-bandgap ($E_g = 0.7$ eV) PbS-CQD solar cells compared to the proposed STPV cell

Power sources	V_{oc}(V)			J_{sc}(mA cm^{-2})			FF ratio			PCE (η (%))		
	This work	[64]	[65]	**This work**	[64]	[65]	**This work**	[64]	[65]	**This work**	[64]	[65]
1300 K	0.36	0.27	-	0.26	0.16	-	0.45	0.55	-	11.3	6	-
AM 1.5	0.50	0.31	0.49	48.9	37.01	34.48	0.79	0.56	0.61	20.20	6.39	10.47

TPV efficiency η of 11.3% is achievable at 1300 K. To our knowledge, such absorptance features, high PCE value and efficient hybrid conversion values were not earlier reported.

Figure 7 summarizes the characteristics for the proposed hybrid STPV cell at various conditions. The J_{sc}, V_{oc}, and PCE calculated values for the hybrid CQDs cell are shown in Fig. 7b under blackbody radiation at various temperatures (T_B). The values calculated at $T_B = 1300$ K are discussed in Table 2. The TPV conversion performance is considerably enhanced by increasing the temperature of the power source. While the TPV conversion efficiency is 11.3% at 1300 K, the value increases to 15.58% at 2400 K. Figure 7c describes the TPV efficiency (η) as a function of blackbody source temperature and short-cutoff wavelength of the filter λ_1. The results show that cell efficiency increases with temperature T_B increase and with filter bandwidth decrease (λ_1 increase). Consequently, adequate filter band and high temperature are typically required to achieve optimal TPV efficiency. Lastly, by changing the fill ratio (f_i) of NSs and the grating height (H), while maintaining other geometric parameters constant, the impact of the two most significant geometric parameters (H and f_i) on the solar cell conversion efficiency, is investigated. As illustrated in Fig. 7d, the solar PCE has been plotted as a fill ratio and grating height function, with H changing from 60 to 180 nm and f_i altering from 1.8 to 10.7%. The fill ratio significantly impacts the PCE when an ideal H is selected. Furthermore, once the H is lowered (< 100 nm), the influence on device performance becomes minor, and the PCE can be increased only to ~ 18%.

Conclusion

Based on plasmonic metamaterials MTMs, a new ultrathin PbS-CQDs hybrid cell is proposed. The proposed design showcases a nearly perfect active absorption, achieving over 80% absorption across a bandwidth of more than 1.47 µm, and covering the spectrum from visible to near-infrared wavelengths. A strong overlap of plasmonic resonance waves usually leads to a broadband response and a high absorptance. The structure shows a J_{sc} of 48.9 mA cm^{-2} and 6.93 mA cm^{-2} under power sources of solar AM 1.5 and blackbody ($T_B = 2400$ K), yielding PCEs of 15.58% and 20.20%, in that order. To our knowledge, this value has not been precedented to date, in these classes of cells. The impact of varying plasmonic mechanisms and plasmonic MTM dimensions on the absorptance processes is examined. Moreover, it is found that a high efficiency occurs when the different plasmonic processes are combined within the ultrathin active layer. High performance in active absorptance and PCE are demonstrated by this design, which is also readily adaptable to other thin-solar cell technologies. These findings provide new ideas to improve the photovoltaic and thermophotovoltaic properties of a new generation of hybrid and ultrathin QD solar cells.

Acknowledgements JMN thanks the Natural Sciences and Engineering Research Council of Canada Discovery Grant (RGPIN-2020-07016). FC acknowledges support from Italian Ministry of Education and Research (MIUR) in the framework of the Forelab project (Departments of Excellence). AC thanks Universite Amar Telidji de Laghouat for the continued support.

Author Contribution O. B.: Conceptualization; Methodology; Investigation; Writing—Original Draft; Formal analysis; Software & Validation. F. B.: Conceptualization; Writing—Original Draft; Supervision; Investigation; Formal analysis; Validation; Software; Writing-review & editing. A. C.: Supervision, Validation and Writing-review; Project administration & Funding acquisition. F. C.: Validation and Writing-review & editing H. S. H.: Validation and Writing-review & editing. J-M. N.: Validation and Writing-review & editing; K. Y.: Validation and Writing-review & editing.

Funding Universite Amar Telidji de Laghouat for continued support,AC,Italian Ministry of Education and Research (MIUR) in the framework of the Forelab project (Departments of Excellence),FC,Natural Sciences and Engineering Research Council of Canada Discovery Grant,JMN,(RGPIN-2020-07016)

Data Availability No datasets were generated or analysed during the current study.

Declarations

Competing interests The authors declare no competing interests.

References

1. Lu H, Carroll GM, Neale NR, Beard MC (2019) Infrared quantum dots: progress, challenges, and opportunities. ACS Nano

13(2):939–953. https://doi.org/10.1021/ACSNANO.8B09815/ASSET/IMAGES/MEDIUM/NN-2018-098153_0009.GIF
2. Song JH, Jeong S (2017) Colloidal quantum dot based solar cells: from materials to devices. Nano Converg 4(1):1–8. https://doi.org/10.1186/S40580-017-0115-0/FIGURES/5
3. Mamiyev Z, Balayeva NO (2023) PbS nanostructures: a review of recent advances. Materials Today Sustainability 21:100305. https://doi.org/10.1016/J.MTSUST.2022.100305
4. Saive R (2021) Light trapping in thin silicon solar cells: a review on fundamentals and technologies. Prog Photovoltaics Res Appl 29(10):1125–1137. https://doi.org/10.1002/pip.3440
5. Murri R, Tucci M, Serenelli L, de Iuliis S, Caputo D, de Cesare G (2013) Light trapping in thin silicon solar cells. In: Silicon based thin film solar cells, pp 395–473. https://doi.org/10.2174/9781608055180113010015
6. Cho C, Song JH, Kim C, Jeong S, Lee JY (2017) Broadband light trapping strategies for quantum-dot photovoltaic cells (>10%) and their issues with the measurement of photovoltaic characteristics. Sci Rep 7(1):1–9. https://doi.org/10.1038/s41598-017-17550-4
7. Ullah I, Hossain MA, Armghan A, Rana MS, Al Asad MA (2023) The optoelectronic enhancement in perovskite solar cells using plasmonic metal-dielectric core-shell and nanorod nanoparticles. Opt Quantum Electron 55(11):1–22. https://doi.org/10.1007/S11082-023-05252-3/METRICS
8. Ullah I, Saghaei H, Khan J, Shah SK (2022) The role of plasmonic metal-oxides core-shell nanoparticles on the optical absorption of Perovskite solar cells. Opt Quantum Electron 54(10):1–13. https://doi.org/10.1007/S11082-022-04051-6/METRICS
9. Ullah I et al (2023) Design and analysis of high-efficiency perovskite solar cell using the controllable photonic structure and plasmonic nanoparticles. J Alloys Compd 960:170994. https://doi.org/10.1016/J.JALLCOM.2023.170994
10. Baitiche O, Bendelala F, Cheknane A, Rabehi A, Comini E (2024) Numerical modeling of hybrid solar/thermal conversion efficiency enhanced by metamaterial light scattering for ultrathin PbS QDs-STPV cell". Crystals 14(7):668. https://doi.org/10.3390/CRYST14070668
11. Ullah H, Daud Khan A, Ullah A, Noman M (2017) Plasmonic perfect absorber for solar cell applications. International Conference on Emerging Technologies (ICET), Islamabad, Pakistan, 2016, pp 1–5. https://doi.org/10.1109/ICET.2016.7813268
12. Gupta BD, Sharma AK, Li J (2023) Plasmonics-based optical sensors and detectors. In: Plasmonics-based optical sensors and detectors. Taylor & Francis, NY, pp 1–509. https://doi.org/10.1201/9781003438304
13. Maier SA (2007) Electromagnetics of metals plasmonics: fundamentals and applications. Plasmon Fundam Appl 1–223. https://doi.org/10.1007/0-387-37825-1/COVER
14. Miller CW, Fu Y, Lopez R (2016) Enhancing energy absorption in quantum dot solar cells via periodic light-trapping microstructures. J Opt (United Kingdom) 18(9):094002. https://doi.org/10.1088/2040-8978/18/9/094002
15. Ullah I, Ullah MI, Ma W, Yuan J (2024) Nanotextured highly efficient optical and light trapping strategies using efficient hole transport-free structure for perovskite solar cells. Opt Commun 556:130276. https://doi.org/10.1016/J.OPTCOM.2024.130276
16. Qiao F, Xie Y, He G, Chu H, Liu W, Chen Z (2020) Light trapping structures and plasmons synergistically enhance the photovoltaic performance of full-spectrum solar cells. Nanoscale 12:1269–1280. https://doi.org/10.1039/c9nr08761c
17. Morawiec S, Crupi I (2019) Light trapping by plasmonic nanoparticles. in Sol cells Light Manag Mater Strateg Sustain Elsevier. 277–313. https://doi.org/10.1016/B978-0-08-102762-2.00008-2
18. Ding Y, Chen P, Fan QH, Hou G (2017) Photonic structures for light trapping in thin film silicon solar cells: design and experiment. Coatings 7(12):236. https://doi.org/10.3390/coatings7120236
19. Toan Dang T, Nguyen TK, Le KQ (2017) Revisited design optimization of metallic gratings for plasmonic light-trapping enhancement in thin organic solar cells. Opt Commun 382:241–245. https://doi.org/10.1016/j.optcom.2016.07.080
20. Hara K, Lertvachirapaiboon C, Ishikawa R, Ohdaira Y, Shinbo K, Kato K, Kaneko F, Baba A (2017) Inverted organic solar cells enhanced by grating-coupled surface plasmons and waveguide modes. Phys Chem Chem Phys 19(4):2791–2796. https://doi.org/10.1039/c6cp06931b
21. Chalh M, Vedraine S, Lucas B, Ratier B (2016) Plasmonic Ag nanowire network embedded in zinc oxide nanoparticles for inverted organic solar cells electrode. Sol Energy Mater Sol Cells 152:34–41. https://doi.org/10.1016/j.solmat.2016.03.021
22. Bhattacharya S, John S (2020) Photonic crystal light trapping: beyond 30% conversion efficiency for silicon photovoltaics. APL Photonics 5(2):020902. https://doi.org/10.1063/1.5128664
23. Dada M, Popoola P, Alao A, Olalere F, Mtileni E, Lindokuhle N, Shamaine M (2023) Functional materials for solar thermo-photovoltaic devices in energy conversion applications: a review. Front Energy Res 11:1124288. https://doi.org/10.3389/fenrg.2023.1124288
24. Wang H, Kubo T, Nakazaki J, Segawa H (2017) Solution-processed short-wave infrared PbS colloidal quantum dot/ZnO nanowire solar cells giving high open-circuit voltage. ACS Energy Lett 2(9):2110–2117. https://doi.org/10.1021/acsenergylett.7b00505
25. Lu H, Carroll GM, Neale NR, Beard MC (2019) Infrared quantum dots: progress, challenges, and opportunities. ACS Nano, 13(2):939–953. https://doi.org/10.1021/acsnano.8b09815
26. Böhm ML, Jellicoe TC, Tabachnyk M, Davis NJLK, Wisniveshy-Rocca-Rivarola F, Ducati C, Ehrler B, Bakulin AA, Greenham NC (2015) Lead telluride quantum dot solar cells displaying external quantum efficiencies exceeding 120%. Nano Lett 15(12):7987–7993. https://doi.org/10.1021/acs.nanolett.5b03161
27. Zheng S, Mei X, Chen J, Johansson EMJ, Zhang X (2024) Colloidal quantum dot for infrared-absorbing solar cells: state-of-the-art and prospects. Nano Res Energy 3(1):Article number: e9120095. https://doi.org/10.26599/NRE.2023.9120095
28. Lan X, Voznyy O, Pelayo F, de Arquer G, Liu M, Xu J, Proppe AH, Walters G, Fan F, Tan H, Liu M, Yang Z, Hoogland S, Sargent EH (2016) 10.6% certified colloidal quantum dot solar cells via solvent-polarity-engineered halide passivation. Nano Lett 16(7):4630–4634. https://doi.org/10.1021/acs.nanolett.6b01957
29. Il Kim H, Baek SW, Cheon HJ, Ryu SU, Lee S, Choi MJ, Choi K, Biondi M, Hoogland S, de Arquer FPG, Kwon SK, Kim YH, Park T, Sargent EH (2020) A tuned alternating D–A copolymer hole-transport layer enables colloidal quantum dot solar cells with superior fill factor and efficiency. Adv Mater 32(48):2004985. https://doi.org/10.1002/adma.202004985
30. Ding C, Wang D, Liu D, Li H, Li Y, Hayase S, Sogabe T, Masuda T, Zhou Y, Yao Y, Zou Z, Wang R, Shen Q (2022) Over 15% efficiency PbS quantum-dot solar cells by synergistic effects of three interface engineering: reducing nonradiative recombination and balancing charge carrier extraction. Adv Energy Mater 12(35):2201676. https://doi.org/10.1002/aenm.202201676
31. Balali-Mood M, Naseri K, Tahergorabi Z, Khazdair MR, Sadeghi M (2021) Toxic mechanisms of five heavy metals: mercury, lead, chromium, cadmium, and arsenic. Front Pharmacol 12:643972. https://doi.org/10.3389/FPHAR.2021.643972/BIBTEX

32. Xia H, Zhan L, Xie B (2017) Preparing ultrafine PbS powders from the scrap lead-acid battery by sulfurization and inert gas condensation. J Power Sources 341:435–442. https://doi.org/10.1016/J.JPOWSOUR.2016.12.035
33. Huang P (2024) Lead in the drinking water is still a problem in the U.S. — especially in Chicago. Shots - Health News: 2024cc NPR. https://www.npr.org/sections/health-shots/2024/04/01/1241470280/lead-pipes-plumbing-water-contamination. Accessed 8 Aug
34. Angrand RC, Collins G, Landrigan PJ, Thomas VM (2022) Relation of blood lead levels and lead in gasoline: an updated systematic review. Environ Health 21(1):1–18. https://doi.org/10.1186/S12940-022-00936-X/FIGURES/13
35. SAMCO Technologies (2024) How to remove lead from your industrial water and wastewater. https://samcotech.com/remove-lead-from-industrial-water-wastewater/. Accessed 8 Aug
36. Ahmad I, Asad U, Maryam L, Masood M, Saeed MF, Jamal A, Mubeen M (2023) "Treatment methods for lead removal from wastewater", *Environmental Science and Engineering*, vol. Part F1251:197–226. https://doi.org/10.1007/978-3-031-37327-5_10
37. Marthaler DE (2013) Numerical methods for metamaterial design, vol 127. Springer NY, pp 31–54. https://doi.org/10.1007/978-94-007-6664-8
38. Bendelala F, Cheknane A, Hilal HS, Goumri-Said S (2019) Extremely low-loss broadband thermal infrared absorber based on tungsten metamaterial. J Electron Mater 48(5):3304–3310. https://doi.org/10.1007/s11664-019-07090-0
39. Mahpeykar SM, Wang X (2017) Optoelectronic engineering of colloidal quantum-dot solar cells beyond the efficiency black hole: a modeling approach. In: Physics, simulation, and photonic engineering of photovoltaic devices VI, vol 10099. SPIE OPTO, San Francisco, California, United States, pp 103–112. https://doi.org/10.1117/12.2248289
40. Polyanskiy MN (2024) Refractiveindex.info database of optical constants. Sci Data 11(1):1–19. https://doi.org/10.1038/s41597-023-02898-2
41. Beliaev LY, Shkondin E, Lavrinenko AV, Takayama O (2021) Thickness-dependent optical properties of aluminum nitride films for mid-infrared wavelengths. J Vac Sci Technol A: Vac Surf Films 39(4):Article 043408. https://doi.org/10.1116/6.0000884
42. Köck W, Paschen P (1989) Tantalum-processing, properties and applications. JOM 41(10):33–39. https://doi.org/10.1007/BF03220360/METRICS
43. Xu Y, Murray J, Munday JN (2014) Photonics and plasmonics for enhanced photovoltaic performance. In: Wu J, Wang Z (eds) Quantum dot solar cells. Lecture notes in nanoscale science and technology, vol 15. Springer, NY, pp 349–382. https://doi.org/10.1007/978-1-4614-8148-5_14
44. Movahed HF (2016) Gradient-doped thermophotovoltaic devices based on colloidal quantum dots. [Online]. Available: https://tspace.library.utoronto.ca/handle/1807/72699. Accessed 09 May 2024
45. Werner WSM, Glantschnig K, Ambrosch-Draxl C (2009) Optical constants and inelastic electron-scattering data for 17 elemental metals. J Phys Chem Ref Data 38(4):1013–1092. https://doi.org/10.1063/1.3243762
46. Foteinopoulou S, Devarapu GCR, Subramania GS, Krishna S, Wasserman D (2019) Phonon-polaritonics: enabling powerful capabilities for infrared photonics. Nanophotonics 8(12):2129–2175. https://doi.org/10.1515/nanoph-2019-0232
47. Ni Q, Alshehri H, Yang Y, Ye H, Wang L (2018) Plasmonic light trapping for enhanced light absorption in film-coupled ultrathin metamaterial thermophotovoltaic cells. Frontiers in Energy 12(1):185–194. https://doi.org/10.1007/s11708-018-0522-x
48. Zhang ZM Mechanical engineering series. [Online]. Springer NY, pp 1–722. Available: http://www.springer.com/series/1161
49. West PR, Ishii S, Naik GV, Emani NK, Shalaev VM, Boltasseva A (2010) Searching for better plasmonic materials. Laser Photonics Rev 4(6):795–808. https://doi.org/10.1002/lpor.200900055
50. Guérout R, Lussange J, Chan HB, Lambrecht A, Reynaud S (2013) Thermal casimir force between nanostructured surfaces. Phys Rev A 87(5):052514. https://doi.org/10.1103/PhysRevA.87.052514
51. Elrashidi A, Elleithy K (2022) High performance polymer solar cells using grating nanostructure and plasmonic nanoparticles. Polymers (Basel) 14(5):862. https://doi.org/10.3390/polym14050862
52. Jin Z, Wang A, Zhou Q, Wang Y, Wang J (2016) Detecting trap states in planar PbS colloidal quantum dot solar cells. Sci Rep 6:37106. https://doi.org/10.1038/srep37106
53. Moreels I, Allan G, De Geyter B, Wirtz L, Delerue C, Hens Z (2010) Dielectric function of colloidal lead chalcogenide quantum dots obtained by a Kramers-Krönig analysis of the absorbance spectrum. Phys Rev B Condens Matter Mater Phys 81(23):235319. https://doi.org/10.1103/PhysRevB.81.235319
54. Olaimat MM, Yousefi L, Ramahi OM (2021) Using plasmonics and nanoparticles to enhance the efficiency of solar cells: review of latest technologies. J Opt Soc Am B 38(2):638–651. https://doi.org/10.1364/JOSAB.411712
55. Wang H, Wang L (2015) Tailoring thermal radiative properties with film-coupled concave grating metamaterials. J Quant Spectrosc Radiat Transf 158:127–135. https://doi.org/10.1016/J.JQSRT.2014.11.015
56. Zamkoye II, Lucas B, Vedraine S (2023) Synergistic effects of localized surface plasmon resonance, surface plasmon polariton, and waveguide plasmonic resonance on the same material: a promising hypothesis to enhance organic solar cell efficiency. Nanomaterials 13(15):2209. https://doi.org/10.3390/nano13152209
57. Xuan Y, Zhang Y (2014) Investigation on the physical mechanism of magnetic plasmons polaritons. J Quant Spectrosc Radiat Transf 132:43–51. https://doi.org/10.1016/j.jqsrt.2012.10.020
58. Lee BJ, Wang LP, Zhang ZM (2008) Coherent thermal emission by excitation of magnetic polaritons between periodic strips and a metallic film. Opt Express 16(15):11328–11336. https://doi.org/10.1364/OE.16.011328
59. Wang L, Zhang ZM, Woodruff GW (2010) Effect of magnetic polaritons on the radiative properties of double-layer nanoslit arrays. Journal of the Optical Society of America B 27(12):2595–2604. https://doi.org/10.1364/JOSAB.27.002595
60. Su CS, Fu CJ (2021) Effect of geometric parameters and grazing incidence on magnetic polaritons excited in 1D multi-groove gratings. Sci China Technol Sci 64(8):1589–1598. https://doi.org/10.1007/s11431-020-1779-7
61. Wu S, Wang G, Wang Q, Zhou L, Zhao J, Huang C, Zhu Y (2009) Novel optical transmission property of metal-dielectric multilayered structure. J Phys D Appl Phys. 42(22):225406 https://doi.org/10.1088/0022-3727/42/22/225406
62. Chen G, Han C, Yan L, Li Y, Zhao Y, Zhang X (2019) Simulation and application of external quantum efficiency of solar cells based on spectroscopy. J Semicond 40(12):122701. https://doi.org/10.1088/1674-4926/40/12/122701
63. Bendelala F, Cheknane A, Hilal H (2018) Enhanced low-gap thermophotovoltaic cell efficiency for a wide temperature range based on a selective meta-material emitter. Sol Energy 174:1053–1057. https://doi.org/10.1016/j.solener.2018.10.006
64. Bi Y, Bertran A, Gupta S, Ramiro I, Pradhan S, Christodoulou S, Majji S-N, Akgul MZ, Konstantatos G (2019) Solution processed infrared- and thermo-photovoltaics based on 0.7 eV bandgap PbS colloidal quantum dots. Nanoscale 11(3):838–843. https://doi.org/10.1039/c8nr08755e

65. Li M, Chen S, Xiong K, Wang B, Shah UA, Gao L, Lan X, Zhang J, Hsu HY, Tang J, Song H (2022) Matching charge extraction contact for infrared PbS colloidal quantum dot solar cells. Small 18(1):2105495. https://doi.org/10.1002/smll.202105495

Authors and Affiliations

Oussama Baitiche[1] · Fathi Bendelala[1] · Ali Cheknane[1] · Filippo Costa[2] · Hikmat S. Hilal[3] · Jean-Michel Nunzi[4] · Khadidja Younes[1]

✉ Fathi Bendelala
f.bendellala@lagh-univ.dz

Ali Cheknane
a.cheknane@lagh-univ.dz

Hikmat S. Hilal
hshilal@najah.edu

Jean-Michel Nunzi
nunzijm@queensu.ca

[1] Laboratoire Matériaux, Systèmes Énergétiques, Énergies Renouvelables et Gestion de l'Énergie (LMSEERGE), Université Amar Telidji de Laghouat, Bd Des Martyrs BP37G, 03000 Laghouat, Algeria

[2] Department of Information Engineering, University of Pisa, Pisa, Italy

[3] Chemistry Department, SSERL, An-Najah National University, Nablus P400, Palestine

[4] Department of Physics, Engineering Physics and Astronomy, Department of Chemistry, Queen's University, Kingston, ON K7L3N6, Canada